



City Research Online

City St George's, University of London

Citation: Cai, B., Li, K. & Fu, F. (2023). Flexural behavior of steel fiber-reinforced coal gangue aggregate concrete beams. *Structures*, 52, pp. 131-145. doi: 10.1016/j.istruc.2023.03.172

This is the accepted version of the paper.

This version of the publication may differ from the final published version. To cite this item please consult the publisher's version.

Permanent repository link: <https://openaccess.city.ac.uk/id/eprint/30177/>

Link to published version: <https://doi.org/10.1016/j.istruc.2023.03.172>

Copyright and Reuse: Copyright and Moral Rights remain with the author(s) and/or copyright holders. Copies of full items can be used for personal research or study, educational, or not-for-profit purposes without prior permission or charge, unless otherwise indicated, provided that the authors, title and full bibliographic details are credited, a hyperlink and/or URL is given for the original metadata page and the content is not changed in any way. For full details of reuse please refer to [City Research Online policy](#).

36 performance than concrete frame structures built using natural crushed stone while saving 6.6% of
37 the construction cost [8]. In recent years, the material properties of coal gangue as well as the
38 working performance, mechanical failure mechanisms [9-11], and frost resistance of coal gangue
39 concrete using coal gangue as an aggregate replacement have been studied. Qiu et al. [12]
40 established a freeze-thaw damage evolution model for coal gangue. Ma et al. [13] found that coal
41 gangue as a coarse aggregate in alkali-activated gangue-slag concrete has high compressive strength
42 and good durability and that the coal gangue content should be in the range of 30-50% when used
43 in a freeze-thaw environment. Incorporating steel fiber or slag powder into coal gangue can optimize
44 its mesostructure and reduce the air voids of concrete, which is conducive to the frost resistance of
45 concrete [14]. However, coal gangue as a lightweight aggregate is characterized by high water
46 absorption and low strength; thus, the mechanical properties and durability of coal gangue concrete
47 are worse than those of ordinary concrete under the same conditions [15,16]. Although the
48 mechanical properties of coal gangue concrete are inferior to those of natural aggregate concrete
49 [17,18], coal gangue concrete can be used in practical applications [8].

50 Since Mangat and Hannat [19] applied the theory of composite mechanics to steel fiber
51 reinforced concrete in the 1970s, the theoretical research and engineering applications of steel fiber
52 reinforced concrete have developed rapidly [20]. Fibers can significantly improve the tensile
53 strength, deformation capacity, crack resistance, and durability of ordinary concrete [21-25].
54 Relevant studies have shown that the incorporation of steel fibers into coal gangue concrete can
55 optimize its mesostructure and reduce the air voids of concrete [14].

56 In addition, finite element (FE) analysis is also an effective method to study the structural
57 performance of new material beam members. Gotame et al. [26] performed a nonlinear finite
58 element analysis to evaluate the buckling behavior of corrosion-damaged reinforced concrete beams
59 reinforced with externally bonded fibre reinforced polymer. Aghani et al. [27] performed a nonlinear
60 finite element analysis using ABAQUS software to estimate the long-term response of the reinforced
61 concrete beam. Xu et al. [28] proposed the preparation of highly porous ceramics using coal gangue,
62 coal slime, and coconut palm fibers as raw materials and built an FE model of porous ceramics using
63 ABAQUS to simulate the stress distribution and compressive strength of porous ceramics. Zhang et
64 al. [29] presented an FE model for circular concrete-filled steel tube (CFST) short columns prepared
65 with coal gangue based on ABAQUS, and comparison of the numerical results with experimental
66 data showed that the coal gangue replacement rate and the confinement effect are the main factors
67 affecting the compressive behavior of CFSTs. Previous numerical studies also revealed that the FE
68 software ABAQUS can simulate the mechanical behavior and ultimate loads of various members
69 with very high accuracy. However, there are few studies on FE models of steel fiber reinforced coal
70 gangue concrete beams. To fill the research gap, this study investigated the influence of various
71 parameters on the flexural performance of SFCGC beams with reference to the above case studies
72 and by means of a FEM established in ABAQUS.

73 The flexural properties of concrete beams prepared from coal gangue aggregate were
74 investigated in this study. Four-point bending tests were conducted on 11 beams with different
75 values of the coal gangue replacement rate, steel fiber volume content, rebar ratio, and beam height.
76 The measured failure modes, load-deflection curves, flexural stiffness, ductility, and energy
77 dissipation coefficient of the specimens were analyzed. The principal structure curves and
78 calculation equations of the steel fiber-reinforced coal gangue coarse concrete (SFCGC) beams were
79 obtained by fitting the measurement data, and a nonlinear elastic-plastic finite element model (FEM)

80 of SFCGC was established and validated based on the test results. The validated FEM was used to
 81 conduct a parametric study to investigate the effects of the CGRR, SFVC, and rebar ratio on the
 82 flexural load carrying capacity of SFCGC beams.

83 2. Experimental Tests

84 2.1. Mix design and basic mechanical properties of the materials

85 Natural gravel and coal gangue with particle diameters of 5-12 mm were used to prepare SFOC
 86 and SFCGC beams. Table 1 shows the chemical composition of coal gangue determined by an X-
 87 ray fluorescence (XRF) test. The basic material performance indices are listed in Table 2. The
 88 properties of the fibers are shown in Table 3. Corrugated steel fibers were used in this study.

89 Table 4 shows the mix proportion used to fabricate the specimens following JGJ55-2011 [30]
 90 and CECS38:2004 [31]. Standard test cubes with dimensions of $150 \times 150 \times 150 \text{ mm}^3$ and
 91 $100 \times 100 \times 300 \text{ mm}^3$ were maintained under the same conditions for 28 days, and then used to perform
 92 axial compression and splitting tensile tests according to GB/T 50081-2019 [32]. Tensile strength
 93 tests were conducted on longitudinal rebar samples. The measured mechanical properties of SFOC
 94 and SFCGC are shown in Table 5, and those of rebar are shown in Table 6. **The rebar used in this
 95 study originated from the construction site. It is understood that this batch of steel bars have been
 96 cold-drawn by people on the construction site, so that their strength has been improved, resulting in
 97 higher test results than theoretical results.**

98 **Table 1**

99 Chemical composition of coal gangue.

SiO ₂	Al ₂ O ₃	Fe ₂ O ₃	FeO	BaO	MgO	K ₂ O	Na ₂ O	TiO ₂	P ₂ O ₅	MnO
48.14	48.14	4.59	7.03	7.40	6.53	2.16	3.70	2.31	0.51	0.2

100 **Table 2**

101 Performance indices of shale ceramsite.

Materials	Bulk density(kg/m ³)	Water absorption(%)	Crash index(%)
Natural stone	1500	1.57	6.5
Coal gangue	1205	5.63	10.4

102 **Table 3**

103 Physical properties of steel fibers.

Steel fiber	Length(mm)	Width(mm)	Thickness(mm)	Equivalent diameter(mm)	Aspect ratio	Density(g/cm ³)
CSF	38	1	0.35-0.5	0.76	50	7.8

104 **Table 4**

105 Mixture compositions (Unit:kg/m³).

No.	R%	v _{sf} %	CG	gravel	cement	sand	Pl	W/C
SFOC-1	0	1	0	1155.5	503.7	622.22	5.04	0.40

HSFCGC-1	50	1	577.7	577.8	503.7	622.22	5.04	0.40
SFCGC-0	100	0	1155.5	0	503.7	622.22	5.04	0.40
SFCGC-0.5	100	0.5	1155.5	0	503.7	622.22	5.04	0.40
SFCGC-1	100	1	1155.5	0	503.7	622.22	5.04	0.40
SFCGC-1.5	100	1.5	1155.5	0	503.7	622.22	5.04	0.40

106 Note: In the specimen names, SFOC indicates that R is 0%, that is, ordinary concrete; HSFCGC and
107 SFCGC indicate that R is 50% and 100% respectively; and the number indicates the v_{sf} ; $R = CGRR$;
108 $v_{sf} = SFVC$, CG = the coal gangue coarse aggregate; PI = the plasticizer; W/C = the water-cement
109 ratio.

110 **Table 5**

111 Measured mechanical properties of the concrete.

No.	Axial compressive strength (MPa)	Splitting tensile strength (MPa)	Elastic modulus (GPa)
SFOC-1	47.11	3.53	34.05
HSFCGCC-1	46.62	3.51	33.96
SFCGC-0	35.87	2.44	30.00
SFCGC-0.5	42.31	2.88	33.11
SFCGC-1	46.56	3.48	33.76
SFCGC-1.5	46.83	3.61	33.14

112 **Table 6**

113 Basic parameters of the rebar.

Rebar type	Diameter(mm)	Yield strength(MPa)	Ultimate strength(MPa)	Elastic modulus(GPa)
HRB400	10	513	611	205
HRB400	14	453	568	205
HRB400	18	431	543	213

114 2.2. Specimen parameters

115 The specific parameters of the test beams are shown in Table 7. 11 beams were designed,
116 including 9 SFCGC beams and 2 SFOC beams with a 25-mm-thick protective layer, where the test
117 beam rebar details is shown in Table 8.

118 **Table 7**

119 Design of test beams.

No.	$R\%$	$v_{sf}\%$	$\rho\%$	b/mm	h/mm	h_0/mm	L/mm	L_0/mm
SFOC-2-1	0	1	1.17	150	200	175	2000	1800
SFCGC-1-1	100	1	0.6	150	200	175	2000	1800
SFCGC-2-1	100	1	1.17	150	200	175	2000	1800
SFCGC-3-1	100	1	1.94	150	200	175	2000	1800
HSFCGC-2-1	50	1	1.17	150	200	175	2000	1800
SFCGC-2-0	100	0	1.17	150	200	175	2000	1800
SFCGC-2-0.5	100	0.5	1.17	150	200	175	2000	1800
SFCGC-2-1.5	100	1.5	1.17	150	200	175	2000	1800

SFOC-4-1	0	1	1.12	150	300	275	2000	1800
HSFCGC-4-1	50	1	1.12	150	300	275	2000	1800
SFCGC-4-1	100	1	1.12	150	300	275	2000	1800

120 Note: ρ = rebar ratio; b = beam section width; h = beam section height; h_0 = the effective height; L
121 = beam length; L_0 = beam effective length. In the specimen names, the first symbol “1, 2, 3, 4”
122 indicates 0.6%, 1.17%, 1.94%, 1.12%, respectively; and the second symbol indicates v_{sf} .

123 **Table 8**

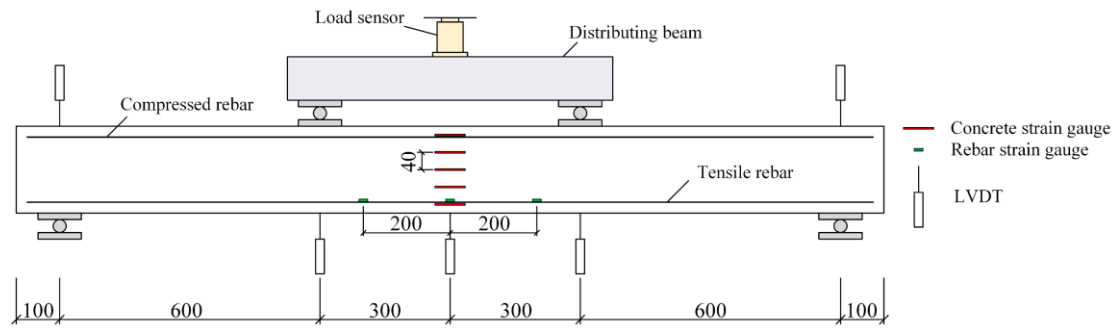
124 Rebar details for all test beams.

Specimen	Longitudinal rebar		Stirrups
	Tensile rebar	Compressed rebar	
SFOC-2-1	2H14	2H8	H8@75
SFCGC-1-1	2H10	2H8	H8@75
SFCGC-2-1	2H14	2H8	H8@75
SFCGC-3-1	2H18	2H8	H8@75
HSFCGC-2-1	2H14	2H8	H8@75
SFCGC-2-0	2H14	2H8	H8@75
SFCGC-2-0.5	2H14	2H8	H8@75
SFCGC-2-1.5	2H14	2H8	H8@75
SFOC-4-1	3H14	2H8	H8@75
HSFCGC-4-1	3H14	2H8	H8@75
SFCGC-4-1	3H14	2H8	H8@75

125 Note: “H8”, “H10”, “H14”, “H18” denote ribbed rebar (the rebar type HRB400) with nominal
126 diameters of 8, 10, 14 and 18 mm, respectively. “@75” denotes the spacing between the stirrups
127 along the test beam is 75mm.

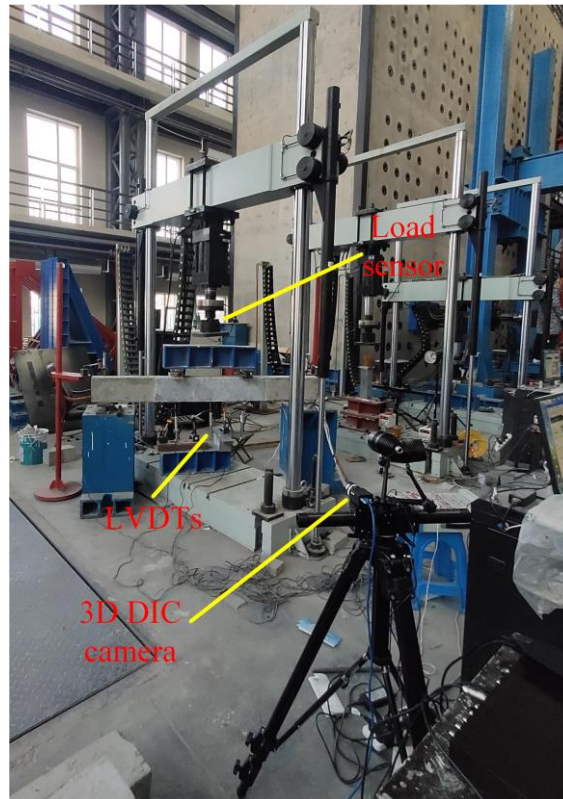
128 2.3. Loading Scheme

129 The specimens were loaded using a 500-kN hydraulic servo pressure testing machine (Fig. 1)
130 in a two-point symmetric manner. A 5-kN preload was first applied to the specimens, after which
131 the load was zeroed and a new load was applied at a speed of 2 kN per minute to obtain a cumulative
132 load of 5 kN per stage, where each stage being has held for 5 minutes. After the rebar yielded, the
133 loading rate was adjusted to 1 kN per minute with a load increment of 2 kN per stage. The load was
134 continuously applied until specimen failure. The transverse strain of the concrete was measured
135 using both conventional adhesive strain gauges, and digital image correlation (DIC), on the two
136 sides of each beam. DIC is a precise, non-contact, and non-interferometric optical method used for
137 measuring the displacement/deformation of a structural element/material subjected to external
138 loading. DIC is based on the principles of continuum mechanics (rigid body mechanics) [33]. The
139 test system is shown in Fig. 2.



140
141

Fig. 1. Schematic diagram of loading device of the specimen.



142
143

Fig. 2. DIC test preparation.

144 3. Test results and analysis

145 3.1. Experimental phenomenon

146 **Fig. 3 shows the failure mode of SFOC-2-1 and SFCGC-2-1.** The failure mode and crack
 147 pattern of the SFCGC beam were similar to those of the SFOC beam, i.e., flexural failure in both
 148 cases, as shown in Fig. 3. For the SFCGC beam, at a load of $0.3F_u$, there were clear signs of vertical
 149 cracks around the mid-span. After the formation of bending cracks around the mid-span, new
 150 vertical cracks started to propagate near the neutral layer as the load increased. During the formation
 151 of these new cracks, the cracks had already formed around the mid-span continued to propagate
 152 over the entire height of the SFCGC beam and the SFOC beam, approaching the compression zone.
 153 In addition, the already-formed cracks began to expand just below the loading point. The concrete

154 on the top surface was damaged upon failure.



155

156

(a)



157

158

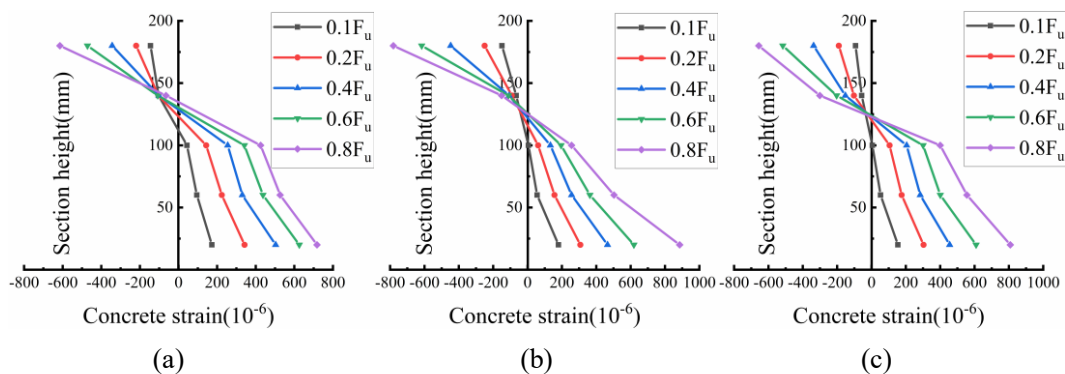
(b)

159

Fig. 3. Loaded state of specimens: (a) SFOC-2-1; (b) SFCGC-2-1.

160 3.2. Plane-section assumption

161 The plane-section assumption is fundamental for performing calculations based on flexural
162 theory based on flexural theory. Fig. 4 shows the distribution of the concrete strain along the section
163 height for different CGRRs. The concrete strain is approximately linear in the section height at all
164 loading levels, which is consistent with the plane-section assumption. The height of the cross-
165 sectional neutral axis is slightly lower for SFCGC beam than SFOC beam under the same loading
166 level.



167

168

169

170

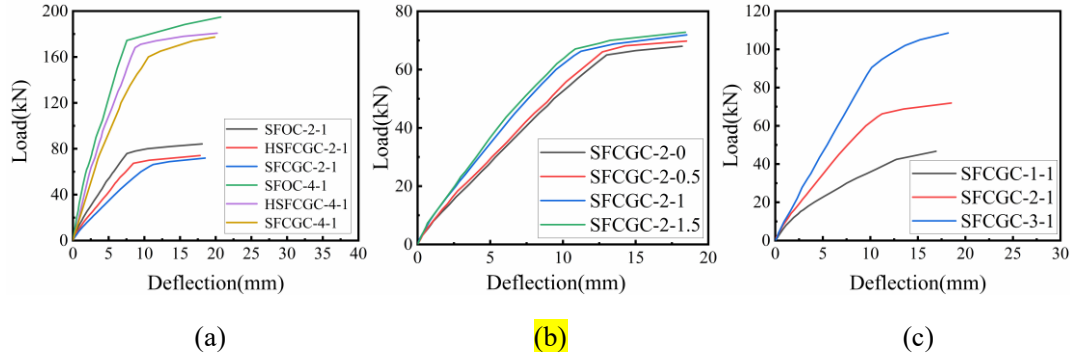
Fig. 4. Distribution of the concrete strain along the section height under different CGRRs: (a) SFOC-2-1; (b) SFCGC-2-1 and (c) SFCGC-2-1.

171 3.3. Load-deflection curve

172 Fig. 5 shows the load-deflection curves of the 11 specimens. In the initial stage of loading, the
173 specimen is in the elastic stage, and hence, the deflection basically increases linearly with the load.
174 After concrete cracking, the first turning point appears in the load-deflection curve, leading to a
175 decrease in the flexural stiffness and an increase in the cracks and deflection of the specimen. As
176 the tensile rebars yielded, the second turning point appears in the load-deflection curve. Accordingly,
177 the flexural stiffness of the specimen decreases sharply and its deflection increases rapidly. When

178 the load reaches the peak, the concrete in the compression zone is crushed, and the specimen lost its
179 bearing capacity.

180 Table 9 shows the test results of the specimens. As the beam depth increases from 200 mm to
181 300 mm, the bearing capacity and flexural stiffness of both SFCGC and SFOC beam increase. With
182 increasing CGRR, there is a relatively small reduction in the cracking load of the specimens of 8.8%
183 on average, and relatively large reductions in the yield and ultimate loads of 12.1% and 13.3% on
184 average, respectively. With increasing SFVC, the development of cracks in the SFCGC beam is
185 suppressed, thus substantially increasing the cracking load of the SFCGC beam. The increase in the
186 cracking load of the specimen reaches 58.6% at 1% SFVC, and then slows beyond 1% SFVC.



187
188 (a) (b) (c)
189 **Fig. 5.** Load-deflection curve of specimens under different effects: (a) CGRR; (b) SFVC and
190 (c) Rebar ratio.

191 **Table 9**

192 Test result of specimens.

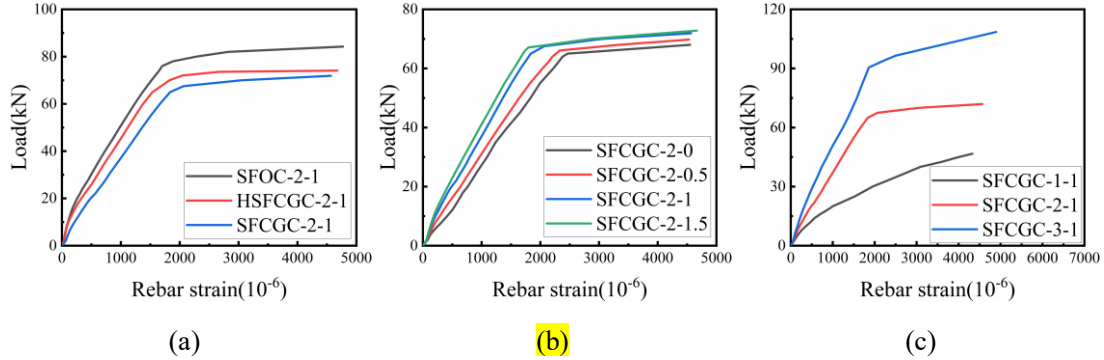
Beam specimens	F_{cr}/kN	ω_{cr}/mm	F_y/kN	ω_y/mm	F_u/kN	ω_u/mm	F_{cr}/F_u	$K_0(kN/mm)$	μ_ω	β
SFOC-2-1	25.50	1.97	76.00	7.65	84.23	18.11	0.30	11.30	2.37	1.53
SFCGC-1-1	15.20	2.67	42.47	12.47	46.67	16.91	0.32	5.19	1.35	1.29
SFCGC-2-1	21.57	2.87	66.27	11.24	71.90	18.52	0.30	7.14	1.65	1.39
SFCGC-3-1	27.80	2.82	90.47	10.14	108.53	18.18	0.27	9.34	1.79	1.31
HSFCGC-2-1	24.93	2.71	67.33	8.48	74.07	17.82	0.33	8.86	2.10	1.47
SFCGC-2-0	13.60	2.17	65.00	13.01	68.00	18.20	0.20	5.60	1.40	1.30
SFCGC-2-0.5	18.34	2.76	66.07	12.72	69.77	18.50	0.26	5.87	1.45	1.32
SFCGC-2-1.5	23.17	2.96	67.07	10.85	72.81	18.42	0.32	7.43	1.70	1.40
SFOC-4-1	64.50	2.10	174.43	7.55	194.75	20.70	0.33	28.63	2.74	1.57
HSFCGC-4-1	64.10	2.56	168.13	8.71	180.70	20.20	0.35	23.54	2.32	1.55
SFCGC-4-1	63.20	3.12	160.04	10.56	177.33	19.85	0.35	20.44	1.88	1.45

193 Note: F_{cr} = the cracking load; ω_{cr} = the cracking deflection; F_y = the yield load; ω_y = the yield
194 deflection; F_u = the ultimate load; ω_u = the ultimate deflection; K_0 = the initial stiffness; μ_ω = the
195 ductility; and β = the energy dissipation coefficient.

196 3.4. Load-rebar strain curve

197 The load-rebar strain curves of the specimens are shown in Fig. 6. The load-rebar strain curve
198 of each beam specimen is similar to its load-deflection curve. The rapid increase in the average post-

199 cracking rebar strain is found to depend on tensile rebar ratio. The average rebar strain increases
 200 rapidly with the increase in rebar ratio. In addition, the rebar strain decreases as the SFVC increases,
 201 because the steel fibers bore a portion of the tension after the beam cracked, thereby reducing the
 202 rebar stress at the same load level, and decreasing the rebar strain. With the increase in CGRR, the
 203 rebar strain increases slightly under the same load level.

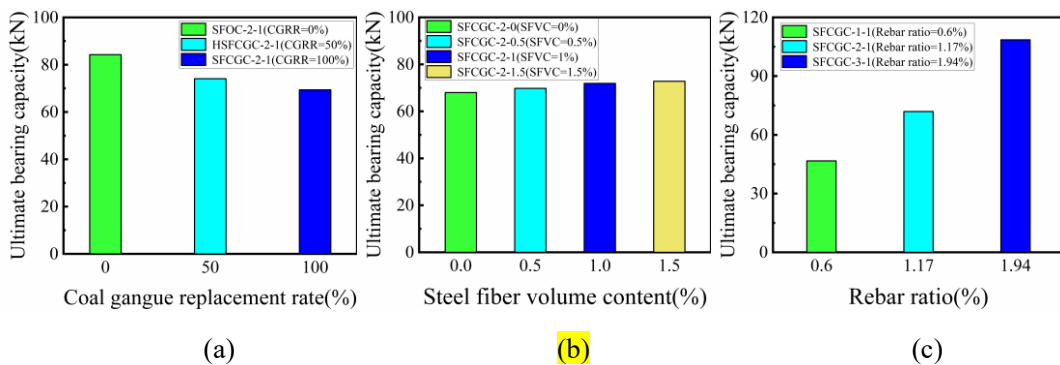


204
 205 (a) (b) (c)
 206 **Fig. 6.** Load-rebar strain curve under different effects: (a) CGRR; (b) SFVC and (c) Rebar
 207 ratio.

208 4. Analysis of influencing factors

209 4.1. Flexural capacity

210 The specimen bearing capacity decreases considerably with increasing CGRR (Fig. 7(a)), This
 211 is due to the fact that the elastic modulus of SFOC is greater than SFCGC (Table 5). With increasing
 212 SFVC, the specimen bearing capacity increases but is not much (Fig. 7(b)), which is due to the
 213 slightly increase compressive strength of the specimen by mixing steel fiber (Table 5). And the
 214 specimen bearing capacity rise dramatically with increasing rebar ratio (Fig. 7(c)).



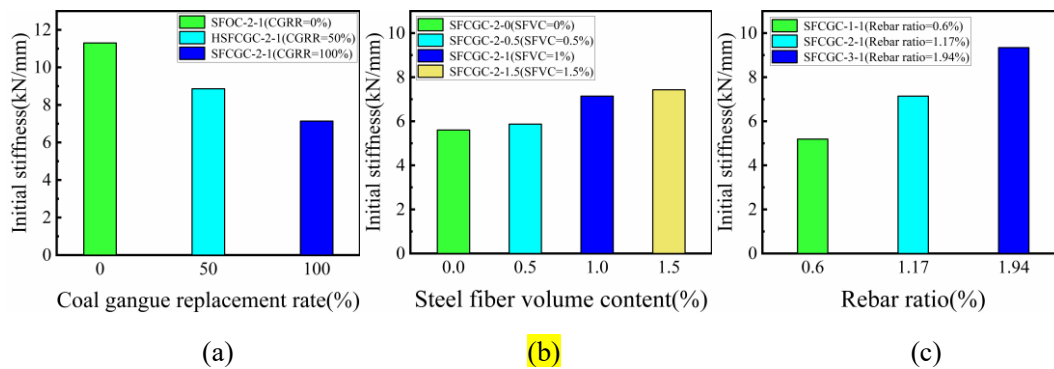
215
 216 (a) (b) (c)
 217 **Fig. 7.** Effects of the investigated variables on bearing capacity: (a) CGRR; (b) SFVC and (c)
 218 Rebar ratio.

219 4.2. Stiffness degradation

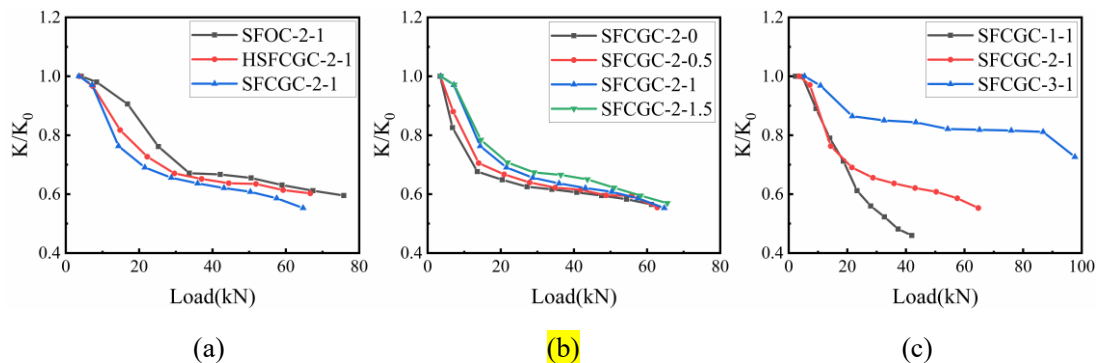
220 The secant stiffness at the point corresponding to $0.4F_u$ in the ascending section of the load-
 221 deflection curve is consistently taken as the initial stiffness in this study, and the results are shown

222 in Table 9. Fig. 8 shows how the CGRR, SFVC, and rebar ratio affect the initial stiffness (denoted
 223 by K_0) of the specimen for SFOC-2-1, SFCGC-2-0, and SFCGC-1-1. The initial stiffness of the
 224 specimen gradually decreases with increasing CGRR and gradually increases with the SFVC and
 225 rebar ratio.

226 Fig. 9 shows how the CGRR, SFVC, and rebar ratio affect the degradation of the specimen
 227 stiffness, where K_0 represents the flexural stiffness at a specimen loading of $0.05 F_u$. Fig. 9(a) and
 228 Table 8 indicate that the stiffness begins to degrade when the load reached approximately 10 kN. As
 229 the load increases from $0.05 F_u$ to $0.67 F_u$, the instantaneous stiffness K of SFOC-2-1, HSFCGC-2-
 230 1, and SFCGC-2-1 degrade by 35.5%, 36.3%, and 38%, respectively. These results show that the
 231 higher the CGRR is, the faster the stiffness degradation and crack development of the SFCGC beam
 232 are, because the lower elastic modulus of the coal gangue aggregate compared to that of natural
 233 crushed stone, rapidly reduces the cross-sectional stiffness of the member. Fig. 9(b) shows that the
 234 incorporated steel fibers delays the stiffness degradation of the member to a certain extent, and when
 235 the load increases to approximately 23 kN ($0.3 F_u$), the steel fibers no longer play a pronounced role
 236 in delaying the stiffness degradation of the member, which is because the member at this moment
 237 had entered a crack development stage and the role of steel fibers in limiting the cracking of the
 238 member is weakened. Fig. 9(c) shows that increasing the rebar ratio slows down the rate of stiffness
 239 degradation of the SFCGC beams given the same cross-section.



240
 241
 242 **Fig. 8.** Effects of the investigated variables on the initial stiffness: (a) CGRR; (b) SFVC and (c)
 243 Rebar ratio.



244
 245
 246 **Fig. 9.** Rigidity degenerations of specimens under different effects: (a) CGRR; (b) SFVC and (c)
 247 Rebar ratio.

248 4.3. Ductility analysis

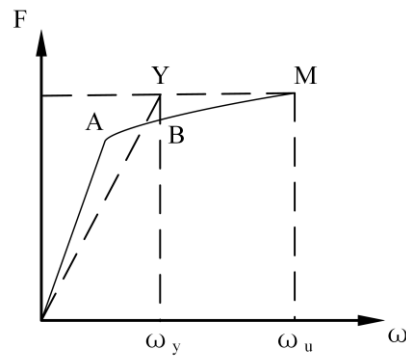
249 The deflection ductility coefficient was used as a measure of the ductility of the specimen in

250 this study and was calculated as follows:

$$251 \quad \mu_{\omega} = \frac{\omega_u}{\omega_y} \quad (1)$$

252 where ω_u is the peak mid-span deflection, ω_y is the mid-span deflection corresponding to yield point,
 253 and the value is determined by the energy equivalence method (Fig. 10).

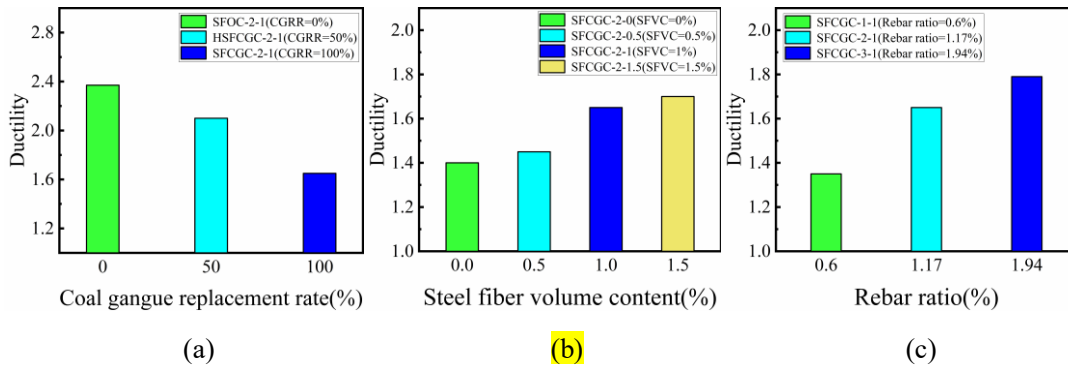
254 The ductility of each specimen was calculated with Equation (1), and the results are outlined
 255 in Table 9. Fig. 11 shows the effects of the CGRR, SFVC, and rebar ratio on the specimen ductility.
 256 The specimen ductility decreases by 11.4% and 30.4% at CGRRs of 50% and 100%, respectively.
 257 This result implies that the specimen ductility decreased increasingly rapidly with increasing CGRR.
 258 The specimen ductility trends upward with the SFVC, with an average increase of 13.2%. The
 259 specimen ductility increases significantly with the rebar ratio.



260

261

Fig. 10. Schematic diagram for calculating ductility coefficient.



262

263

Fig. 11. Effects of the investigated variables on the specimen ductility: (a) CGRR; (b) SFVC and
 265 (c) Rebar ratio.

266 4.4. Energy dissipation coefficient analysis

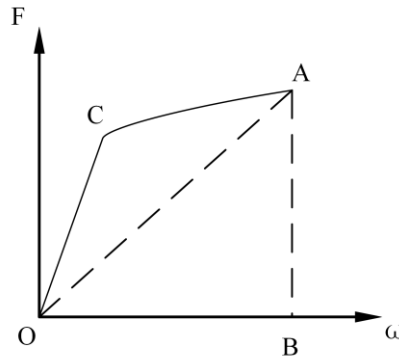
267 The capacity of a member to dissipate energy determines the level of protection provided to a
 268 building in an earthquake. In this study, the magnitude of the energy dissipation of the specimen
 269 was denoted by β :

$$270 \quad \beta = \frac{S_{OCAB}}{S_{OAB}} \quad (2)$$

271 where S_{OCAB} is the area enclosed by the load-deflection curve and the coordinate axis at the peak

272 load, which is the actual energy dissipation, S_{OAB} is the area of the triangle enclosed by the origin,
 273 the ultimate load point and the coordinate axis (Fig. 12).

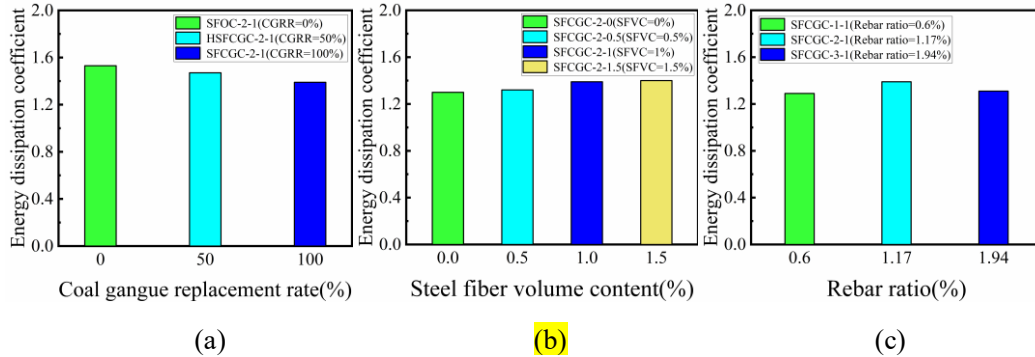
274 The energy dissipation coefficient of each specimen was calculated according to Equation (2),
 275 and the results are given in Table 9. Fig. 13(a) shows that the energy dissipation of the specimens
 276 decreases slightly (by 10%) with increasing CGRR. As the coal gangue aggregate contained more
 277 cracks and pores than natural gravel, compression, and closure of cracks during loading, increase
 278 the energy absorption of the specimen and lower the energy dissipation. Fig. 13(b) shows that the
 279 energy dissipation coefficient of SFCGC beams increases slightly with increasing SFVC. As shown
 280 in Fig. 13(c), as the rebar ratio increases, the energy dissipation coefficient does not change
 281 appreciably and first increased and then decreased overall. Therefore, the use of a high rebar ratio
 282 both improves the bearing capacity and reduces the energy dissipation of SFCGC beams.



283

284

Fig. 12. Calculation of the energy dissipation coefficient.



285

286

287

288

Fig. 13. Effects on the investigated variables on the energy dissipation coefficient of the specimens: (a) CGRR; (b) SFVC and (c) Rebar ratio.

289

4.5. Calculation of the cracking load

290

The cracking load (F_{cr}) can be calculated is as follows [37]:

291

$$F_{cr} = \frac{2M_{cr}}{L} \quad (3)$$

292

$$M_{cr} = f_t b (h - x_{cr}) \left(\frac{h - x_{cr}}{2} + \frac{2x_{cr}}{3} \right) + 2\alpha_E f_t A_s \left(h - \frac{x_{cr}}{3} \right) \quad (4)$$

293

$$x_{cr} = \frac{1 + \frac{2\alpha_E A_s}{bh}}{1 + \frac{\alpha_E A_s}{bh}} \cdot \frac{h}{2} \quad (5)$$

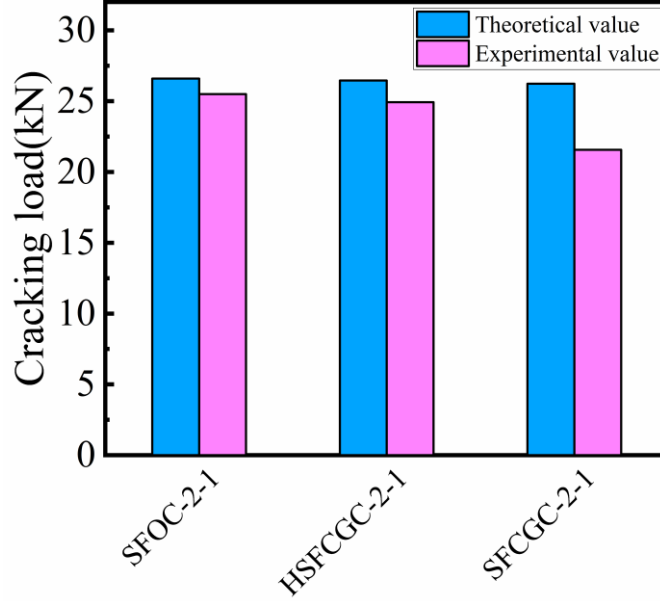
294

295

296

297

where M_{cr} is the cracking moment of the specimen; L is the pure bending region of the beam (=600mm in this study); f_t is the tensile strength of concrete; h is the beam height; and x_{cr} is the effective depth of the concrete compression zone when concrete cracks occur; and α_E is the ratio of elastic modulus of rebar to that of concrete.



298

299

300

301

302

303

304

305

Fig. 14. Comparison between theoretical value and experimental value on the cracking load of the specimens on different CGRR

Fig. 14 exhibits the comparison between the theoretical value and experimental value on the cracking load of the beam specimens with an SFVC of 1% and a rebar ratio of 1.17% and different CGRR. It can be seen that the error between the two is small, and the calculation accuracy of the formula is good. It is proved that Equation (3) and Equation (4) can well predict the cracking load and moment of SFCGC beam.

306

4.6. Calculation of the ultimate load

307

The ultimate load (F_u) can be calculated is as follows [37]:

308

$$F_u = \frac{2M_u}{L} \quad (6)$$

309

$$M_u = f_y A_s \left(h_0 - \frac{x}{2} \right) \quad (7)$$

310

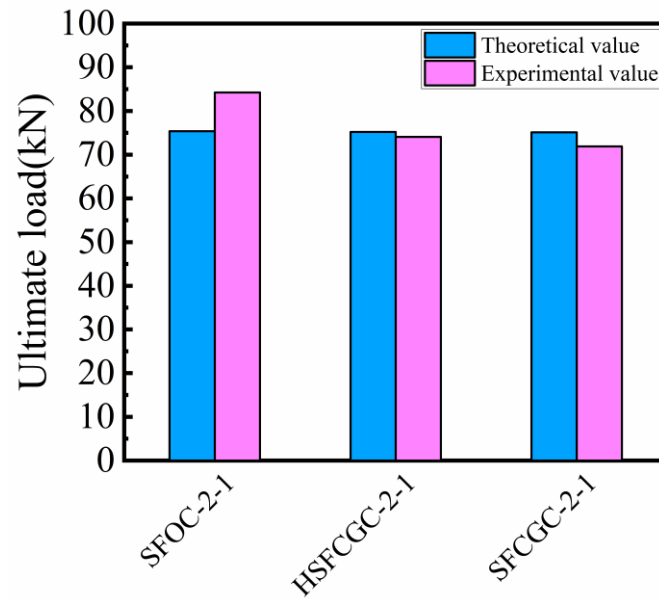
$$x = \frac{f_y A_s}{\alpha_1 f_c b} \quad (8)$$

311

312

where M_u is the ultimate moment of the specimen; α_1 is a coefficient related to concrete strength (i.e. 1.0 for concrete grades \leq C50, and 0.94 for concrete grades \geq C80); f_c is the axial compressive

313 strength of concrete cube; and x is the concrete compression zone depth, assuming the equivalent
314 rectangular block.



315
316 **Fig. 15.** Comparison between theoretical value and experimental value on the cracking load of the
317 specimens on different CGRR

318 Fig. 15 exhibits the comparison between the theoretical value and experimental value on the
319 ultimate load of the beam specimens with an SFVC of 1% and a rebar ratio of 1.17% and different
320 CGRR. It can be seen that the error between the two is small, and the calculation accuracy of the
321 formula is good. It is proved that Equation (6) and Equation (7) can well predict the ultimate load
322 and moment of SFCGC beam.

323 6. Finite element simulation

324 6.1. FEM model and meshing

325 The core SFCGC was modeled using eight-node 3D solid elements with reduced integration
326 (C3D8R) [34]. The rebar and steel fiber were constructed using T3D2 elements. T3D2 is a 2-node
327 linear displacement element, where each node has three translational degrees of freedom. The
328 specifications of the overall model are shown in Fig. 16. Based on a convergence analysis, the mesh
329 size of all beams was chosen as 20mm, where the mesh distribution of the model is shown in Fig.
330 17.

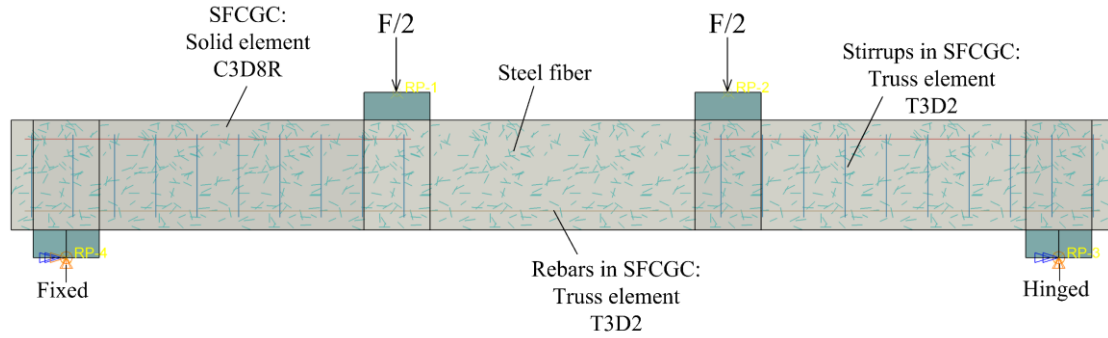


Fig. 16. FEM.

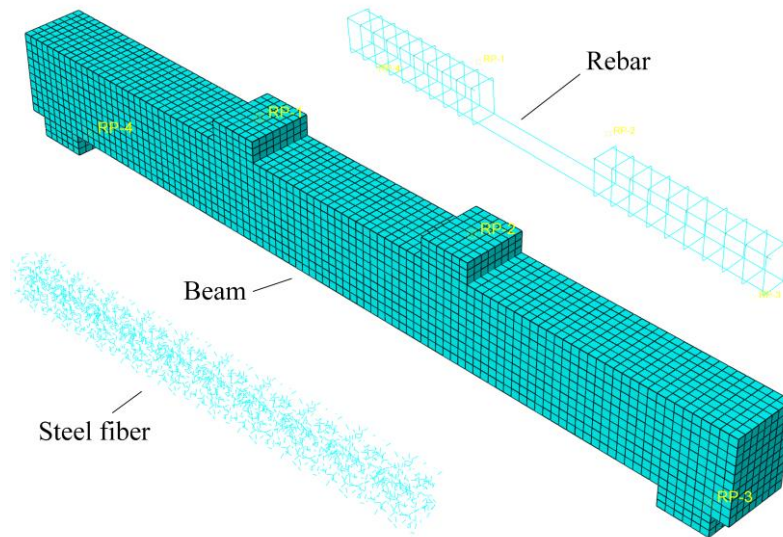


Fig. 17. FEM meshing.

6.2. Model parameters

6.2.1. Constitutive model of concrete

The stress-strain curves under tension and compression are defined differently within the concrete damaged plasticity (CDP) model. The stress-strain curve of concrete under uniaxial compression obtained by uniaxial compression tests on prisms is shown in Fig. 18, and its overall shape is found similar to that of ordinary concrete. Therefore, the full stress-strain curve of ordinary concrete described by Equation (9) [35] was used to fit the constitutive equation of SFCGC.

$$y = \begin{cases} ax + (3 - 2a)x^2 + (a - 2)x^3, & 0 \leq x \leq 1 \\ \frac{x}{b(x-1)^2 + x}, & x > 1 \end{cases} \quad (9)$$

where a is the parameter for fitting the rising section of the stress-strain curve, reflecting the change of concrete deformation modulus; b is the parameter for fitting the declining section of the stress-strain curve, reflecting the size of the area of the declining section curve; x is the ratio of strain to

346 peak strain (i.e. $x=\varepsilon/\varepsilon_p$); and y is the ratio of stress to peak stress (i.e. $y=\sigma/\sigma_p$).

347 The parameters a and b were obtained by curve fitting, as shown in Table 10. Both a and b
 348 decrease as CGRR increases, indicating that the higher the CGRR is, the lower the elastic modulus
 349 and plastic deformation capacity are, which is consistent with the data presented in Table 5. As the
 350 SFVC increases, a increases and b decreases because in the ascending section of the curve, the
 351 cracks are in the stable development stage, and the steel fibers across the cracks play a role in
 352 blocking cracks and slowing crack propagation. Thus, a higher SFVC results in a stronger crack-
 353 blocking effect, a fuller curve, and a larger a . In the descending section of the curve, the cracks are
 354 in the instability and propagation stage. The pull-out force on the steel fibers between the cracks
 355 slows the disintegration of the cement paste, flattening the descending section of the curve. Thus,
 356 increasing the SFVC increases the number of fibers between cracks, resulting in a flatter curve and
 357 a smaller b . Based on the trend of parameters a and b , a fitted regression analysis of a and b was
 358 performed using a linear equation to obtain the fitting curve shown in Fig. 19, and Equations (10)-
 359 (13) show the fitting parameters a and b for the obtained constitutive equation of the SFCGC under
 360 uniaxial compression as a function of the CGRR and SFVC.

361 Since it is necessary to investigate the concrete cracking and characterize the crack
 362 development after concrete cracking, the constitutive equation of SFCGC under tension is
 363 determined using the energy criterion (i.e., stress-fracture energy) for concrete failure [36].

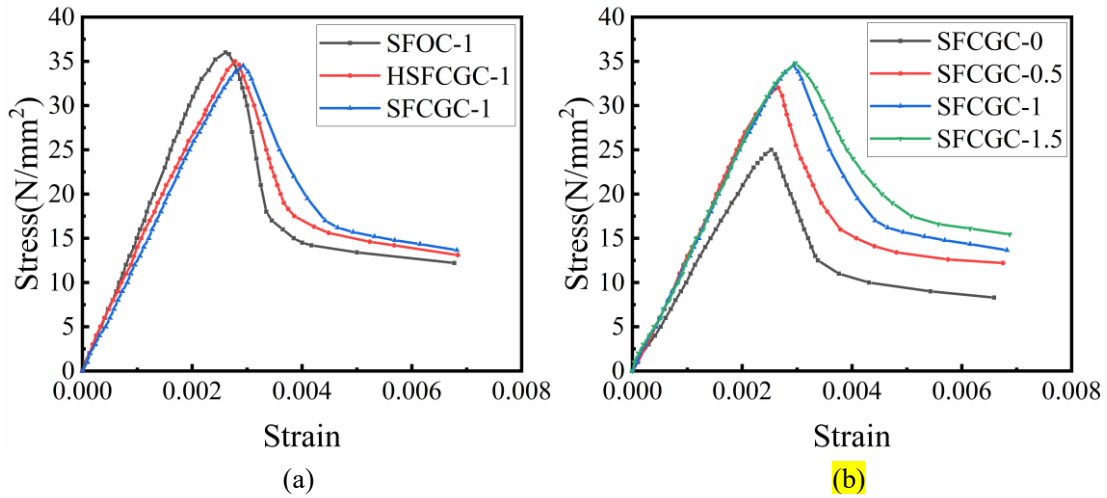
364 The CDP model requires five additional parameters: the flow potential eccentricity; a viscosity
 365 parameter that is a measure of the viscoplastic regularization (μ); the ratio of the second stress
 366 invariant for the tensile meridian to that for the compressive meridian, such that the maximum
 367 principal stress is negative (K_c); the ratio of the initial equibiaxial compressive yield stress to the
 368 initial uniaxial compressive yield stress (σ_{b0}/σ_{c0}) and the dilation angle in degrees (ψ). The
 369 corresponding parameter values were set as 0.1, 0.0005, 0.6667, 1.16, and 30° for SFCGC material
 370 [29].

371
$$a = -0.001371R + 0.6373 \quad (10)$$

372
$$b = -0.05212R + 11.82 \quad (11)$$

373
$$a = 0.08912v_{sf} + 0.4051 \quad (12)$$

374
$$b = -5.825v_{sf} + 12.72 \quad (13)$$



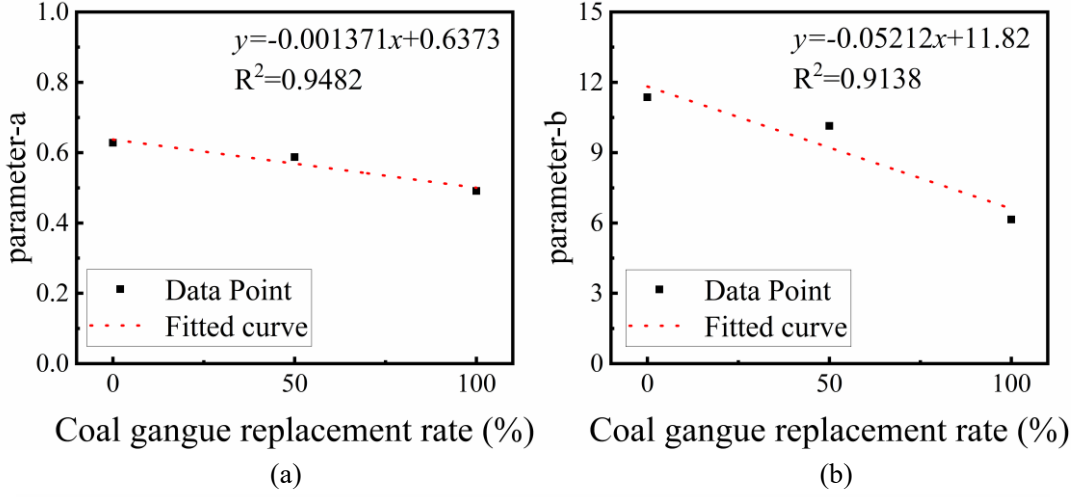
377 **Fig. 18.** Effect of compressive stress-strain curves of the SFCGC: (a) CGRR and (b) SFVC.

378 **Table 10**

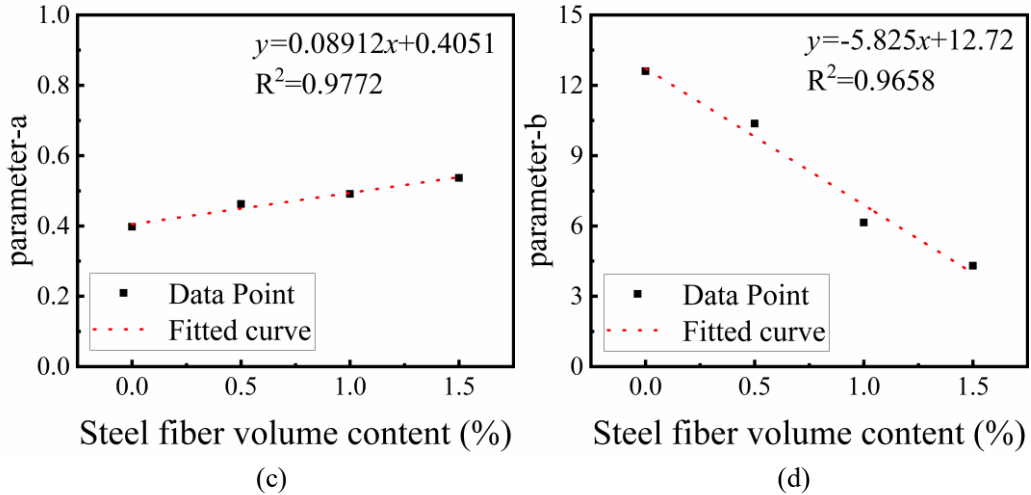
379 Fitting parameters of the uniaxial compressive constitutive equation of concrete.

parameters	SFOC-1	HSFCGC-1	SFCGC-1	SFCGC-0	SFCGC-0.5	SFCGC-1.5
a	0.63	0.59	0.49	0.39	0.46	0.54
b	11.36	10.14	6.481	12.6	10.37	4.30

380



381
382



383
384

385 **Fig. 19.** Fitted curves to relate the parameters a and b with the CGRR and SFVC: (a) Fitted curve
386 of the relationship between the parameter a and the CGRR; (b) Fitted curve of the relationship
387 between the parameter b and the CGRR; (c) Fitted curve of the relationship between the parameter
388 a and the SFVC and (d) Fitted curve of the relationship between the parameter b and the SFVC.

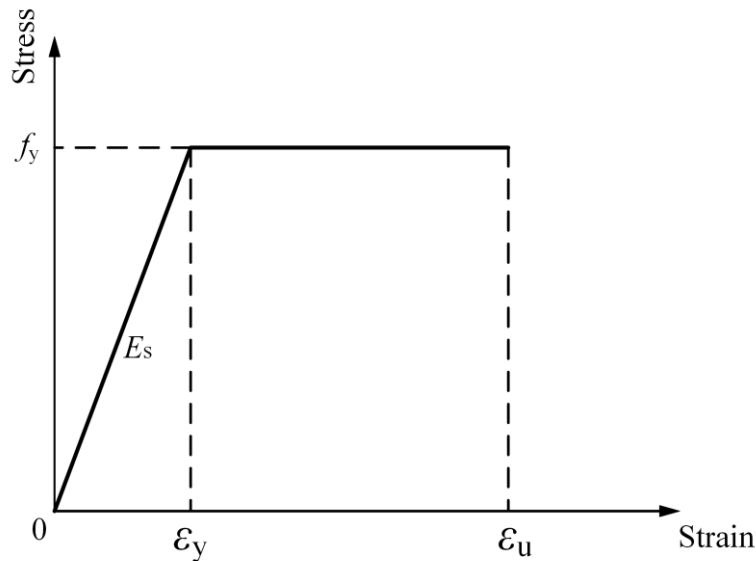
389 6.2.2. Constitutive model of rebar

390 The damage inflicted on the reinforced concrete elements results in the deformation of the
391 rebar and steel fiber mainly remaining in the yield plateau range. Neglecting yield hardening, two
392 fold ideal elastic-plastic model (Fig. 20) according to GB 50010-2010 [37] was used to describe the
393 steel fibers and rebar, where the stress-strain relationship is shown in Equation (14):

$$394 \sigma_p = \begin{cases} E_s \varepsilon_s, & \varepsilon \leq \varepsilon_y \\ f_y, & \varepsilon > \varepsilon_y \end{cases} \quad (14)$$

395 where σ_p = rebar stress, ε_s = rebar strain, ε_y = the yield strain of rebar, f_y = the yield strength of the

396 rebar, and E_s = the elastic modulus of rebar.



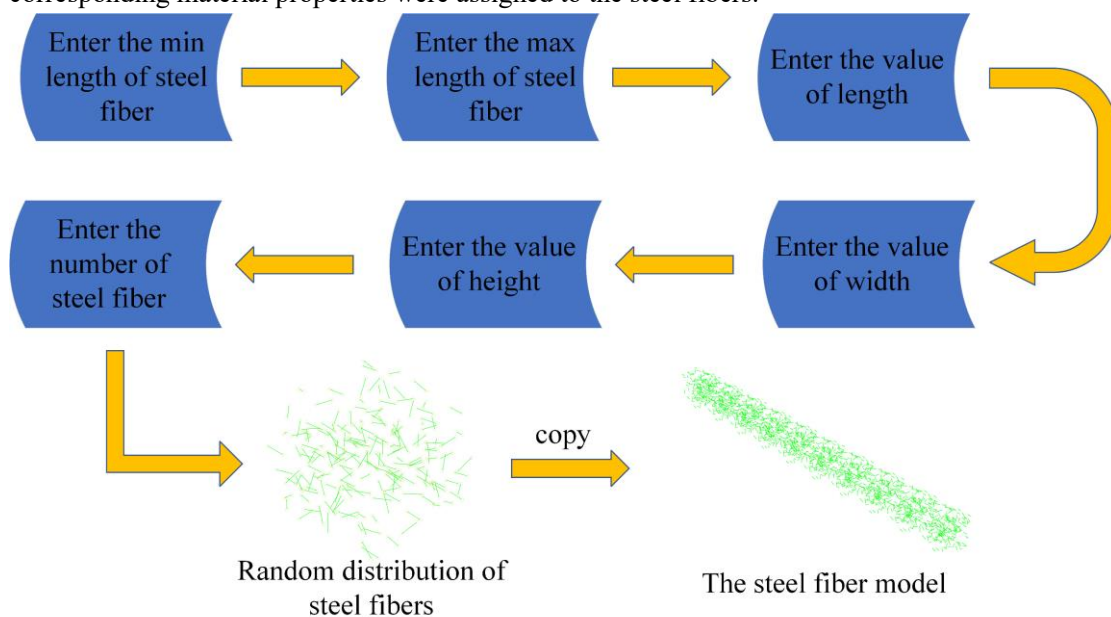
397

398

Fig. 20. Stress-strain relationship for rebars.

399 6.2.3. Steel fiber model

400 The computer code for the randomly distributed steel fiber model was written in Python and
401 imported into ABAQUS. An independent steel fiber model was formed by setting the length of steel
402 fibers, the size of a specific region, and the number of steel fibers in that region. According to the
403 dimensions of the specimen in this study, a beam was divided into 10 equal parts, with the length,
404 width, and height of each region being 200 mm, 150 mm, and 200 mm, respectively. Fig. 21 is a
405 flow chart showing the modeling procedure for the steel fiber, which was finally embedded in the
406 FEM of the SFCGC beam, as shown in Fig. 16. After the modeling was completed, the
407 corresponding material properties were assigned to the steel fibers.



408

409

Fig. 21. Flow chart for the modeling procedure for the steel fibers.

410 **6.3. Interaction**

411 Embedded constraints were applied between the rebar cage and the SFCGC beam as well as
412 between the steel fibers and the SFCGC beam. The SFCGC beam was the main region, and the rebar
413 cage and steel fibers were separate built-in regions. Binding constraints were set between the
414 supports and the beam. The four steel block supports were coupled to RP1, RP2, RP3, and RP4,
415 respectively, so that the degrees of freedom (DOFs) of the supports were controlled by these four
416 constraint points.

417 **6.4. Boundary conditions and load application**

418 The boundary conditions of the FEM of the SFCGC beam prepared with coal gangue aggregate
419 were chosen to be consistent with the test conditions. Simply supported boundary conditions were
420 applied to the supports. The centers of the two beam supports were set as RP3 and RP4, respectively
421 (Fig. 16), and the two supports were set as rigid bodies. The DOFs of RP3 were $U1=U2=0$, and the
422 DOFs of RP4 were $U1=U2=U3=0$. External loads were applied to the two steel blocks at the top of
423 the beam by displacement.

424 **6.5. Model validation**

425 **6.5.1. The validation of the load-deflection curves**

426 To ensure the reliability of the developed numerical model, the simulation results obtained
427 using the FEM were compared with the experimentally obtained values in Fig. 22 and Table 11. The
428 difference between the simulated and experimental load-deflection curves over the entire loading
429 process is approximately 10%; this good agreement shows that the flexural performance of SFCGC
430 beams can be effectively simulated using the developed modeling method.

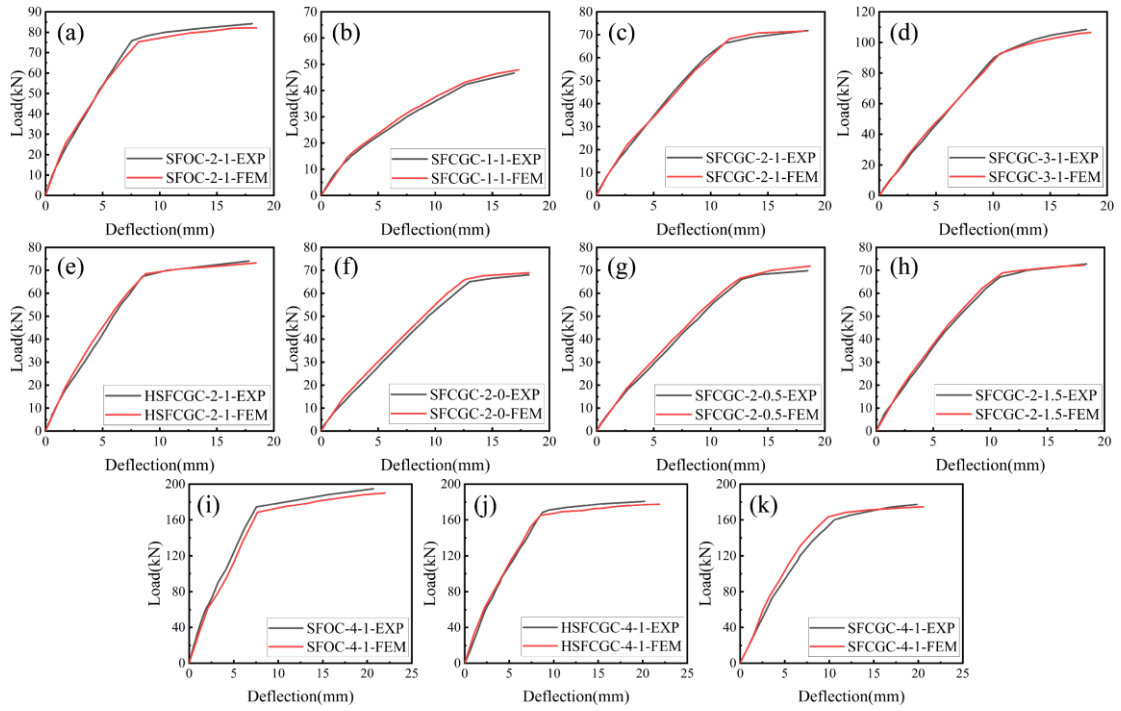


Fig. 22. The comparison of the load-deflection curves calculated by the FEM with the experimental results.

431
 432
 433
 434

435 **Table 11**

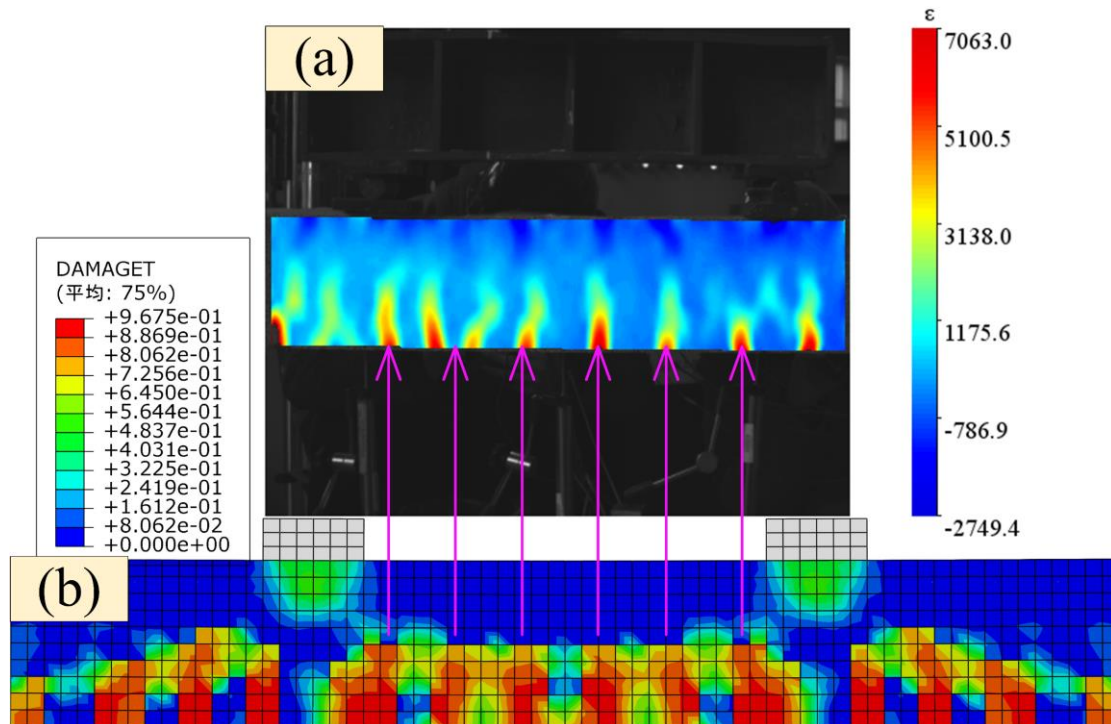
436 Simulated and tested results of load and deflection.

Specimens	$F_{cr}(kN)$			$\omega_{cr}(mm)$			$F_y(kN)$			$\omega_y(mm)$			$F_u(kN)$			$\omega_y(mm)$		
	F_{exp}	F_{simu}	$\frac{F_{exp}}{F_{simu}}$	ω_{exp}	ω_{simu}	$\frac{\omega_{exp}}{\omega_{simu}}$	F_{exp}	F_{simu}	$\frac{F_{exp}}{F_{simu}}$	ω_{exp}	ω_{simu}	$\frac{\omega_{exp}}{\omega_{simu}}$	F_{exp}	F_{simu}	$\frac{F_{exp}}{F_{simu}}$	ω_{exp}	ω_{simu}	$\frac{\omega_{exp}}{\omega_{simu}}$
SFOC-2-1	25.50	26.00	0.98	1.97	1.79	1.10	75.81	75.27	1.01	7.65	8.15	0.94	84.23	82.21	1.02	18.11	18.47	0.98
SFCGC-1-1	15.20	14.71	1.03	2.67	2.32	1.15	42.47	43.17	0.98	12.75	12.59	1.01	46.67	47.89	0.97	16.91	17.32	0.98
SFCGC-2-1	21.57	22.12	0.98	2.87	2.68	1.07	66.27	68.21	0.97	11.24	11.63	0.97	71.90	71.63	1.00	18.52	18.21	1.02
SFCGC-3-1	27.80	26.83	1.04	2.82	2.57	1.10	90.47	92.84	0.97	10.14	10.61	0.96	108.53	106.49	1.02	18.19	18.54	0.98
HSFCGC-2-1	24.93	24.64	1.01	2.71	2.36	1.15	67.33	68.43	0.98	8.48	8.75	0.97	74.07	73.24	1.01	17.82	18.43	0.97
SFCGC-2-0	13.60	12.95	1.05	2.17	1.72	1.26	65.00	66.18	0.98	13.01	12.77	1.02	68.00	68.87	0.99	18.20	18.22	1.00
SFCGC-2-0.5	18.34	18.63	0.98	2.76	2.64	1.05	66.07	66.52	0.99	12.72	12.59	1.01	69.77	71.88	0.97	18.50	18.71	0.99
SFCGC-2-1.5	23.17	22.24	1.04	2.96	2.67	1.11	67.07	68.88	0.97	10.85	11.06	0.98	72.81	72.26	1.01	18.42	18.22	1.01
SFOC-4-1	64.50	61.63	1.05	2.10	2.09	1.00	174.43	168.46	1.04	7.55	7.66	0.99	194.75	190.03	1.02	22.70	22.00	1.03
HSFCGC-4-1	64.10	62.89	1.02	2.56	2.28	1.12	168.13	165.06	1.02	8.71	8.50	1.02	180.70	177.42	1.02	20.20	21.86	0.92
SFCGC-4-1	63.20	60.49	1.04	3.12	2.59	1.20	160.04	163.28	0.98	10.56	9.87	1.07	173.30	174.44	1.02	19.85	20.57	0.96

437 Note: F_{exp} = the test result of the load; F_{simu} = the simulated result of the load; ω_{exp} = the test result of the deflection; ω_{simu} = the simulated result of the deflection.

438 **6.5.2. The validation of the transverse strain**

439 The FEM developed in this study can also be used to take into account differences between the
440 tensile and compressive properties of materials and simulate irreversible degradation of the stiffness
441 due to damage. Two damage coefficients, DAMAGEC and DAMAGET, were defined according to
442 GB 50010-2010 [37] to reflect the development of cracks. Fig. 23(a) presents a contour plot of the
443 transverse strain of SFCGC beam processed by DIC software, and Fig. 23(b) shows the development
444 of cracks in the SFCGC beam (CGC-2) and the corresponding FEM. The crack development is
445 effectively simulated using the FEM. The crack strain development locations of the two are similar,
446 with the maximum crack strain occurring near the loading point.



447
448 **Fig. 23.** Comparison between experimental and simulated results.

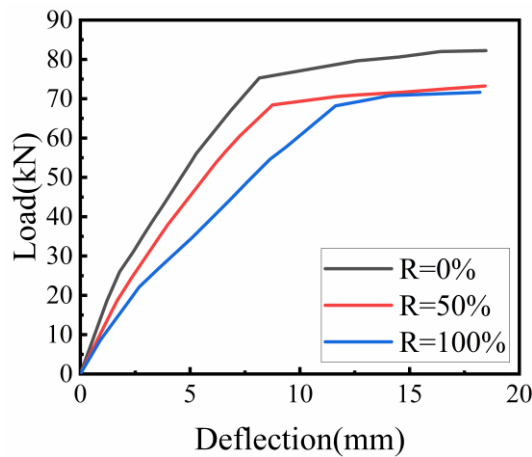
449 **6.6. Parametric study**

450 The validated FEM was used to carry out a parametric study to quantify the effect of different
451 parameters on the flexural performance of SFCGC beams.

452 **6.6.1. Coal gangue replacement rate**

453 The simulation load-deflection curve of elements with different CGRRs is shown in Fig. 24.
454 The results present in Fig. 22 and Table 11 shows that compared with the results for SFOC beams,
455 the cracking load, yield load, and ultimate load of SFCGC beams decrease by 14.9%, 9.4%, and
456 12.9%, respectively, for 100% CGRR and by 5.2%, 9.1%, and 11%, respectively, for 50% CGRR;

457 however, the CGRR does not have a significant effect on the ultimate displacement.

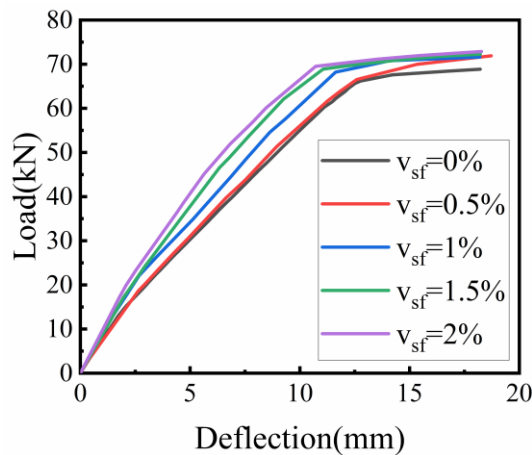


458
459

Fig. 24. Simulation results obtained for different CGRRs.

460 6.6.2. Steel fiber volume content

461 The flexural performances of SFCGC beams with different SFVCs (0, 0.5%, 1%, 1.5%, and
462 2%) were compared. The load-deflection curves are shown in Fig. 25. Compared with the results
463 obtained for beams without steel fibers, increasing the SFVC has a significant influence on the
464 cracking load but a minimal impact on the yield load, ultimate load, and ultimate displacement of
465 the member. In particular, the ultimate displacement and ultimate load do not change significantly
466 as the SFVC increases from 1% to 2%. Therefore, an excessively large SFVC does not significantly
467 improve the force performance of the member while increasing the self-weight of the member due
468 to the incorporation of an excessively large number of fibers. An SFVC of 1% is reasonable
469 considering the advantages offered by lightweight coal gangue concrete.



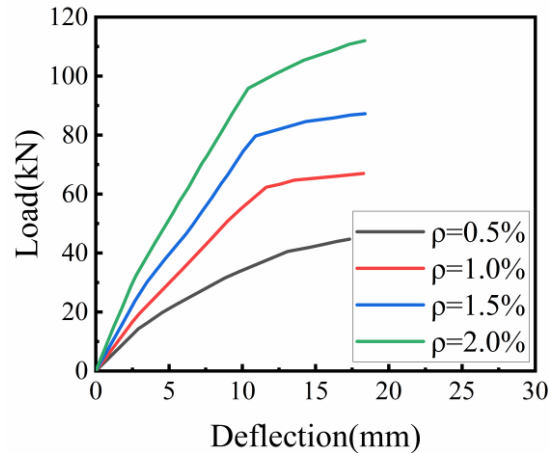
470
471

Fig. 25. Simulation results obtained for different SFVCs.

472 6.6.3. Rebar ratio

473 The simulated load-deflection curves obtained for rebar ratios of 0.5%, 1.0%, 1.5%, and 2.0%
474 are shown in Fig. 26. With increasing rebar ratio, the ultimate load of SFCGC beam increases
475 significantly but the increase of deflection is less. For SFCGC beams with lower load-carrying

476 capacity than SFOC beams, the load-carrying capacity of SFCGC beams can be improved by
477 increasing the rebar ratio.



478
479

Fig. 26. Simulation results obtained for different rebar ratios.

480 7. Conclusion

481 In this study, four-point bending test was conducted on 9 SFCGC beams and 2 SFOC beams.
482 The test parameters were the CGRR, SFVC, rebar ratio, and beam height. The structural properties
483 of the beams, including the flexural stiffness, load-carrying capacity, deformation capacity, cracking
484 behavior, ductility, and energy dissipation, were investigated. The SFCGC beams had comparable
485 structural properties to those of the SFOC beams. The experimental results were compared with
486 those obtained from the FE simulations. The main results of this study are summarized as below.

487 1) The incorporation of coal gangue aggregates reduces various mechanical properties of the
488 concrete, but the strength of SFCGC beams can be made similar to that of SFOC beams by
489 increasing the rebar ratio and adjusting the mix proportions. Based on the data of axial compression
490 tests on prisms, an equation is proposed to predict the compressive stress-strain constitutive
491 relationship of concrete considering the influence of the CGRR and SFVC.

492 2) Comparing with SFOC beams, SFCGC beams exhibit low flexural performance, but their strains
493 along the section height still meet the plane section assumption, and their cracking load, yield load,
494 and ultimate load decrease by 8.8%, 12.1%, and 13.3%, respectively, on average.

495 3) The incorporation of steel fibers effectively delays the development of cracks in SFCGC beams.
496 When the SFVC reaches 1%, the cracking load of SFCGC beams increases by 58.6%, whereas the
497 yield load and ultimate load are minimally affected. When the SFVC exceeds 1%, the cracking load
498 of the specimen increases at a slower rate. For optimal utilization of steel fibers, the optimal SFVC
499 of SFCGC beams should not be greater than 1%.

500 4) The bearing capacity, stiffness, ductility, and energy dissipation capacity of the SFCGC beams
501 decrease with increasing CGRR and increase with the SFVC, and the CGRR and SFVC have a
502 relatively large influence on the stiffness and ductility. As the rebar ratio increases, the energy
503 dissipation capacity of SFCGC beams first increases and then decreases, and the bearing capacity,
504 stiffness, and ductility of the specimens are enhanced significantly. And the flexural load capacity
505 of SFCGC beam is significantly increased with the increase of beam height.

506 5) An equation for predicting the constitutive relationship of SFCGC is presented by fitting the test
507 results. The comparative analysis of the test and FE results show that the established FEM can

508 predict the SFCGC beam flexural performance both reliably and accurately, where there is less than
509 10% error between the predicted and test results. The influences of the parameters of the CGRR,
510 SFVC, and rebar ratio were analyzed in terms of their effects on the bearing capacity. It is found
511 that the bearing capacity of SFCGC beams is slightly lower than that of SFOC beams; however, the
512 crack resistance and bearing capacity of SFCGC beams can be enhanced by incorporating steel
513 fibers and increasing the rebar ratio.

514 **Data Availability**

515 Some or all data, models, or codes that support the findings of this study are available from the
516 corresponding author upon reasonable request.

517 **Declaration of Competing Interest**

518 The authors declare that they have no known competing financial interests or personal
519 relationships that could have appeared to influence the work reported in this paper.

520 **Acknowledgments**

521 This research was financially supported by the Foundation of China Scholarship Council (No.
522 201805975002), and a scientific research projects from the Education Department of Jilin Province
523 (JJKH20210279KJ). The authors wish to acknowledge the sponsors. However, any opinions,
524 findings, conclusions and recommendations presented in this paper are those of the authors and do
525 not necessarily reflect the views of the sponsors.

526 **Reference**

- 527 [1] Quero X, Izquierdo M, Monfort E, Álvarez E, Font O, Moreno T, Alastuey A, Zhuang X, Lu W,
528 Wang Y. Environmental characterization of burnt coal gangue banks at Yangquan, Shanxi Province,
529 China. *International Journal of Coal Geology* 2008; 75(2), 93-104.
530 <https://doi.org/10.1016/j.coal.2008.04.003>
- 531 [2] Dong Z, Xia J, Fan C, Cao J. Activity of calcined coal gangue fine aggregate and its effect on
532 the mechanical behavior of cement mortar. *Construction and Building Materials* 2015; 100, 63-69.
533 <https://doi.org/10.1016/j.conbuildmat.2015.09.050>
- 534 [3] Huang G, Ji Y, Li J, Hou Z, Dong Z. Improving strength of calcinated coal gangue geopolymer
535 mortars via increasing calcium content. *Construction and Building Materials* 2018; 166, 760-768.
536 <https://doi.org/10.1016/j.conbuildmat.2018.02.005>
- 537 [4] Salguero F, Grande J. A, Valente T, Garrido R, De la Torre, M. L., Fortes J. C, Sánchez, A.
538 Recycling of manganese gangue materials from waste-dumps in the Iberian Pyrite Belt–Application
539 as filler for concrete production. *Construction and Building Materials* 2014; 54, 363-368.
540 <https://doi.org/10.1016/j.conbuildmat.2013.12.082>

- 541 [5] Karimaei M, Dabbaghi F, Sadeghi-Nik A, Dehestani M. Mechanical performance of green
542 concrete produced with untreated coal waste aggregates. *Construction and Building Materials* 2020;
543 233, 117264. <https://doi.org/10.1016/j.conbuildmat.2019.117264>
- 544 [6] Yao Z, Fang Y, Kong W, Huang X, Wang X. Experimental study on dynamic mechanical
545 properties of coal gangue concrete. *Advances in Materials Science and Engineering* 2020; 2020.
546 <https://doi.org/10.1155/2020/8874191>
- 547 [7] Gao S, Zhao G, Guo L, Zhou L, Yuan K. Utilization of coal gangue as coarse aggregates in
548 structural concrete. *Construction and Building Materials* 2021; 268, 121212.
549 <https://doi.org/10.1016/j.conbuildmat.2020.121212>
- 550 [8] Zhou X.G. Application of fully spontaneous combustion coal clinoptilolite in high-rise frame
551 structure residential building. *Building Block & Block Construction* 1997; 22–24.
- 552 [9] Li D, Song X, Gong C, Pan Z. Research on cementitious behavior and mechanism of pozzolanic
553 cement with coal gangue. *Cement and Concrete Research* 2006; 36(9), 1752-1759.
554 <https://doi.org/10.1016/j.cemconres.2004.11.004>
- 555 [10] Zhang N, Sun H, Liu X, Zhang J. Early-age characteristics of red mud–coal gangue
556 cementitious material. *Journal of Hazardous Materials* 2009; 167(1-3), 927-932.
557 <https://doi.org/10.1016/j.jhazmat.2009.01.086>
- 558 [11] Yi C, Ma H, Zhu H, Li W, Xin M, Liu Y, Guo Y. Study on chloride binding capability of coal
559 gangue based cementitious materials. *Construction and Building Materials* 2018; 167, 649-656.
560 <https://doi.org/10.1016/j.conbuildmat.2018.02.071>
- 561 [12] Qiu J, Zhou Y, Vatin N. I, Guan X, Sultanov S, Khemarak K. Damage constitutive model of
562 coal gangue concrete under freeze-thaw cycles. *Construction and Building Materials* 2020; 264,
563 120720. <https://doi.org/10.1016/j.conbuildmat.2020.120720>
- 564 [13] Ma H, Zhu H, Wu C, Chen H, Sun J, Liu J. Study on compressive strength and durability of
565 alkali-activated coal gangue-slag concrete and its mechanism. *Powder Technology* 2020; 368, 112-
566 124. <https://doi.org/10.1016/j.powtec.2020.04.054>
- 567 [14] Luo D, Wang Y, Zhang S, Niu D, Song Z. Frost resistance of coal gangue aggregate concrete
568 modified by steel fiber and slag powder. *Applied Sciences* 2020; 10(9), 3229. [10.3390/app10093229](https://doi.org/10.3390/app10093229)
- 569 [15] Li Y, Yao Y, Liu X, Sun H, Ni W. Improvement on pozzolanic reactivity of coal gangue by
570 integrated thermal and chemical activation. *Fuel* 2013; 109, 527-533.
571 <https://doi.org/10.1016/j.fuel.2013.03.010>
- 572 [16] Karagöl F, Yegin Y, Polat R, Benli A, Demirboğa R. The influence of lightweight aggregate,
573 freezing-thawing procedure and air entraining agent on freezing-thawing damage. *Structural*
574 *Concrete* 2018; 19(5), 1328-1340. <https://doi.org/10.1002/suco.201700133>
- 575 [17] Zhang Y, & Ling T. C. Reactivity activation of waste coal gangue and its impact on the
576 properties of cement-based materials-a review. *Construction and Building Materials* 2020; 234,
577 117424. <https://doi.org/10.1016/j.conbuildmat.2019.117424>
- 578 [18] Hu Q, Fang G. Study on Mechanical Properties of Recycled Concrete Block Mixed with Coal
579 Gangue and Plant Fiber. In *IOP Conference Series: Earth and Environmental Science* 2020; Vol.
580 508, No. 1, p. 012179. [10.1088/1755-1315/508/1/012179](https://doi.org/10.1088/1755-1315/508/1/012179)
- 581 [19] Hanant D.J. *Fiber Cement and Fiber Concrete*. China Architecture & Building Press 1986;
582 Beijing, China.
- 583 [20] Marcos-Meson V, Michel A, Solgaard A, Fischer G, Edvardsen C, Skovhus T. L. Corrosion
584 resistance of steel fibre reinforced concrete-A literature review. *Cement and Concrete Research*

585 2018; 103, 1-20. <https://doi.org/10.1016/j.cemconres.2017.05.016>

586 [21] Park S. H, Kim D. J, Ryu G. S, Koh K. T. Tensile behavior of ultra high performance hybrid
587 fiber reinforced concrete. *Cement and Concrete Composites* 2012; 34(2), 172-184.
588 <https://doi.org/10.1016/j.cemconcomp.2011.09.009>

589 [22] Monetti D. H, Llano-Torre A, Torrijos M. C, Giaccio G, Zerbino R, Martí-Vargas J. R, Serna P.
590 Long-term behavior of cracked fiber reinforced concrete under service conditions. *Construction and*
591 *Building Materials* 2019; 196, 649-658. <https://doi.org/10.1016/j.conbuildmat.2018.10.230>

592 [23] Thomas J, Ramaswamy A. Mechanical properties of steel fiber-reinforced concrete. *Journal of*
593 *materials in civil engineering* 2007; 19(5), 385-392. <http://dyuthi.cusat.ac.in/purl/4537>

594 [24] Banthia N, Gupta R. Influence of polypropylene fiber geometry on plastic shrinkage cracking
595 in concrete. *Cement and concrete Research* 2006; 36(7), 1263-1267.
596 <https://doi.org/10.1016/j.cemconres.2006.01.010>

597 [25] Teng S, Afroughsabet V, Ostertag C. P. Flexural behavior and durability properties of high
598 performance hybrid-fiber-reinforced concrete. *Construction and Building Materials* 2018; 182, 504-
599 515. <https://doi.org/10.1016/j.conbuildmat.2018.06.158>

600 [26] Gotame M, Franklin C. L, Blomfors M, Yang J, Lundgren K. Finite element analyses of FRP-
601 strengthened concrete beams with corroded reinforcement. *Engineering Structures* 2022; 257,
602 114007. <https://doi.org/10.1016/j.engstruct.2022.114007>

603 [27] Aghani K, Afshin H, Abedi K. Finite element-based prediction of the long-term deflection of
604 reinforced concrete beams strengthened with prestressed fiber-reinforced polymers. *Structures* 2022;
605 Vol. 43, pp. 358-373. <https://doi.org/10.1016/j.istruc.2022.06.059>

606 [28] Xu H, Du H, Kang L, Cheng Q, Feng D, Xia S. Constructing straight pores and improving
607 mechanical properties of gangue-based porous ceramics. *Journal of Renewable Materials* 2021;
608 9(12), 2129. [10.32604/jrm.2021.016090](https://doi.org/10.32604/jrm.2021.016090)

609 [29] Zhang Y, Xu Q, Wang Q, Zhou M, Liu H, Guo H. Axial compressive behavior of circular
610 concrete-filled steel tube stub columns prepared with spontaneous-combustion coal gangue
611 aggregate. *Journal of Building Engineering* 2022; 103987.
612 <https://doi.org/10.1016/j.jobbe.2021.103987>

613 [30] Ministry of Housing and Urban-Rural Development, Beijing, China. Specification design of
614 ordinary concrete (JGJ 55-2011). 2011. (in Chinese).

615 [31] China Association for Engineering Construction Standardization, Beijing, China. Technical
616 specification for fiber reinforced concrete structures (CECS38:2004). 2004. (in Chinese).

617 [32] Ministry of Housing and Urban-Rural Development, Beijing, China. Standard for test methods
618 of concrete physical and mechanical properties (GB/T 50081-2019). 2019. (in Chinese).

619 [33] Chu T. C, Ranson W. F, Sutton M. A. Applications of digital-image-correlation techniques to
620 experimental mechanics. *Experimental mechanics* 1985; 25(3), 232-244.

621 [34] Systèmes D. Abaqus analysis user's guide. *Solid (Continuum) Elements* 2014; 6, 2019.

622 [35] Guo Z, Shi X. Reinforced concrete theory and analyse. Tsinghua University Press 2003. (in
623 Chinese)

624 [36] Hillerborg A, Modéer M, Petersson P. E. Analysis of crack formation and crack growth in
625 concrete by means of fracture mechanics and finite elements. *Cement and concrete research* 1976;
626 6(6), 773-781.

627 [37] Ministry of Housing and Urban-Rural Development, Beijing, China. Code for design of
628 concrete structures (GB50010-2010). 2010. (in Chinese).